Promotion of adsorptive and catalytic properties of zeolitic Brønsted acid sites by proximal extra-framework Si(OH)$_x$ groups

Ruixue Zhao [1], Rachit Khare[1], Yang Zhang[1], Maricruz Sanchez-Sanchez[1], Ricardo Bermejo-Deval[1], Yue Liu [1,2] ✉ & Johannes A. Lercher [1,3] ✉

Steric confinement in zeolites influences the catalytic conversion of alkanes. For zeolitic Brønsted acid sites, proximate extra-framework species introduce additional confinement to the pore constraints, enhancing the catalytic activity of alkane cracking. Although extra-framework alumina has been the most studied, here we report the element-specific impact of silica species. By grafting extra-framework silica species close to Brønsted acid sites in H-ZSM-5 zeolite, the binding of bases like pyridine and amines is strengthened via van der Waals interactions with their aryl or alkyl chains. Brønsted acid sites close to extra-framework silica achieve a higher reaction rate of protolytic cracking of *n*-pentane via enthalpic (unlike entropic, as with extra-framework alumina) stabilization of the transition state by 24–51 kJ mol^{-1}. The lower activation energy points to an earlier transition state than in the presence of extra-framework alumina, with a better stabilization of the carbonium ions in the transition state compared to the parent zeolite.

Zeolites are widely used in the chemical and petroleum industry as an acid catalyst for cracking[1,2], isomerization[3] and alkylation[4]. The active sites that catalyse these reactions are the bridging OH groups (SiOHAl) of the zeolites, which act as Brønsted acid sites (BAS)[1–10]. Their acidity is typically adjusted by varying the aluminium (Al) concentration[11–13], introducing cations such as boron or iron[14–16] into the tectosilicate framework and partly exchanging the acid sites with rare-earth metal cations (for example, La^{3+})[17–19].

Molecules adsorb on BAS in zeolites, but also interact with the pores through dispersion forces[20,21]. Typically scaling in intensity with the fit between the sorbate and the sorbent, this non-directed bonding has been shown to be critical for the adsorption and catalytic properties of zeolites[22–25]. It has been demonstrated that the strength of interaction can be subtly modulated by varying the framework structure and via introducing cations at exchange positions or extra-framework species[26–28].

The catalytic activity of BAS in protonic forms of zeolites is an intrinsic property that has been linked to the pore size, the location of the BAS in the pores and to local constraints induced by extra-framework alumina (EFAl) clusters[5,29]. The latter sites have been identified to cause a markedly higher activity[2,12,29–34]. Although some reports have attributed this to an increased acid strength of BAS[12,13,35,36], recent work from our laboratory[29,30] and other groups[28,37–39] ascribed this promotion effect to the confined space of BAS in close proximity to EFAl, establishing that the presence of EFAl stabilizes transition states via increasing the transition entropy[30]. In turn, this implies that the impact of the constraining species should be independent of its chemical nature.

Modification of zeolites by grafting silica species has been used to block BAS on the external surface or at the pore mouth of the zeolite[40]. Synthetically, this is realized through chemical vapour deposition[41] or chemical liquid deposition[42], using silicon sources such as

[1]Technical University of Munich, Department of Chemistry, Catalysis Research Center, Garching, Germany. [2]Shanghai Key Laboratory of Green Chemistry and Chemical Processes, School of Chemistry and Molecular Engineering, East China Normal University, Shanghai, People's Republic of China. [3]Institute for Integrated Catalysis, Pacific Northwest National Laboratory, Richland, WA, USA. ✉e-mail: liuyue@chem.ecnu.edu.cn; johannes.lercher@ch.tum.de

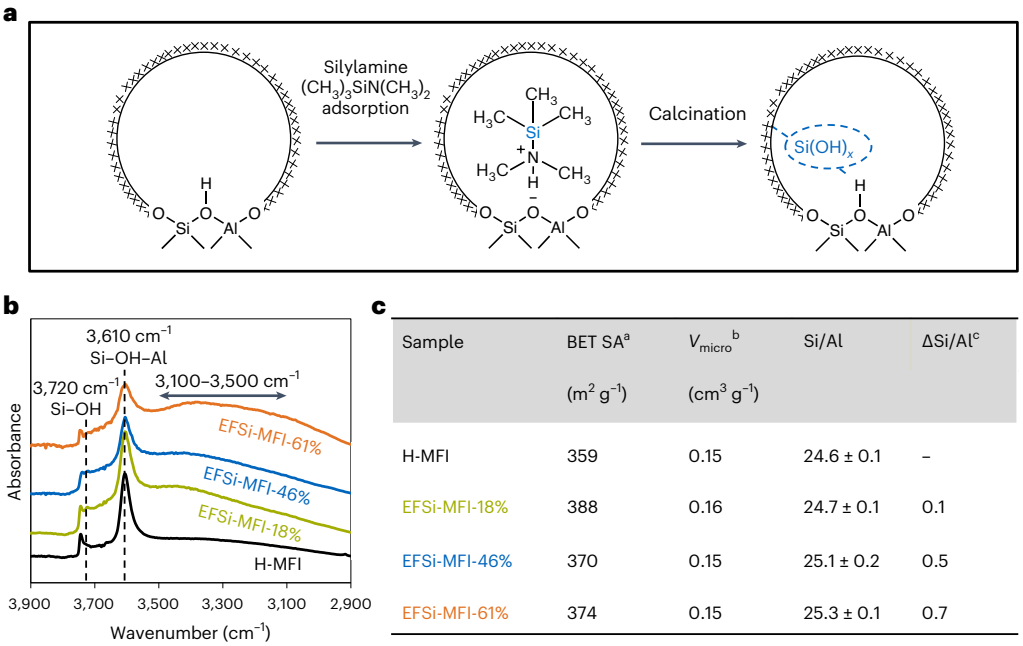

c

Sample	BET SA[a] ($m^2\ g^{-1}$)	V_{micro}[b] ($cm^3\ g^{-1}$)	Si/Al	ΔSi/Al[c]
H-MFI	359	0.15	24.6 ± 0.1	–
EFSi-MFI-18%	388	0.16	24.7 ± 0.1	0.1
EFSi-MFI-46%	370	0.15	25.1 ± 0.2	0.5
EFSi-MFI-61%	374	0.15	25.3 ± 0.1	0.7

Fig. 1 | Grafting EFSi in H-MFI. a, Schematic illustration of EFSi grafting in H-MFI. **b**, Infrared spectra of the OH stretching vibration region of H-MFI and EFSi-MFI samples. All samples were activated at 723 K under vacuum for 1 h; the spectra were collected at 423 K under vacuum. **c**, Physicochemical properties of H-MFI and EFSi-MFI samples. [a]Brunauer–Emmett–Teller surface area. [b]Micropore volume. [c]Increase in Si/Al ratio in EFSi-MFI samples compared with the parent H-MFI.

tetraethoxysilane and tetramethoxysilane. These modifications did not affect the BAS in the zeolite micropores and has been attributed to the fact that the silica precursor is largely unable to enter the pores. If, however, the enhancement in the acid-catalysed alkane and alkene cracking by the EFAl clusters is caused solely by creating local constraints, silica clusters close to BAS should also be able to induce such an effect[29,30,32,37,43].

Therefore, we decided to probe that hypothesis by modifying zeolite BAS using chemically anchored extra-framework silica (EFSi; that is, $Si(OH)_x$). The anchored EFSi is supposed to lead to a more confined environment that is specified near the BAS without changing the general porous system in H-ZSM-5. We report this strategy here, showing that the EFSi clusters in proximity to the BAS indeed enhance the adsorption of base molecules with alkyl chains via van der Waals interactions. The acid-catalysed reaction rate of *n*-pentane cracking is also enhanced via enthalpic stabilization of the transition states, in contrast to EFAl clusters, which involve entropic stabilization of the transition states.

Results

Synthesis, identification and quantification of EFSi-BAS sites

EFSi species were grafted in the pores of the parent H-ZSM-5 sample (named as H-MFI) via a two-step process, first adsorbing *N*,*N*-dimethyltrimethylsilylamine ($(CH_3)_3SiN(CH_3)_2$) on the BAS, followed by linking the silica species on lattice oxygen not associated with the BAS through calcination in air at 823 K (Fig. 1a). The amine group precursor selectively interacted with BAS to form an aminium ion. This was concluded from the decrease in the intensity of the infrared band of the SiOHAl group (3,610 cm^{-1}) and the appearance of the respective N–H vibration (1,620 cm^{-1}) band in the infrared spectrum of the sample exposed to the silylamine (Supplementary Fig. 1)[44,45]. After calcination, the organic part was removed, as shown by the disappearance of the C–H and N–H vibration bands in the infrared spectra (Supplementary Fig. 1). The samples before and after this modification did not show any differences in their X-ray diffractograms and Al NMR spectra (Supplementary Figs. 2 and 3, respectively) and had identical values for their BET surface area (373 ± 15 $m^2\ g^{-1}$) and micropore volume (0.15–0.16 $cm^2\ g^{-1}$; Fig. 1c and Supplementary Fig. 4). A small increase in the Si/Al ratio was observed with increased EFSi grafting, where the modified samples are denoted as EFSi-MFI-*X*% (with *X*% being the portion of EFSi-BAS determined via pyridine titration).

The location, nature and impact of the EFSi on the BAS was first probed using infrared spectroscopy (Fig. 1b). The EFSi-MFI samples showed a higher intensity of the band at 3,720 cm^{-1}. Because this band is characteristic of Si–OH groups in zeolite channels[46–48], we conclude that the majority of the EFSi species are located in the micropores. The intensity of the band at 3,610 cm^{-1} (SiOHAl groups)[46,49] was lower for EFSi-MFI samples compared with H-MFI (Fig. 1b). This decrease is attributed either to a chemical blocking or to a perturbation of the SiOHAl groups by the EFSi (Fig. 1a), suggesting a close proximity between EFSi and SiOHAl groups. A new broad band between 3,100 and 3,500 cm^{-1} suggests that the latter interpretation is more likely, and this broad band is tentatively assigned to SiOHAl hydrogen bonding with Si–OH. Such a shift to lower wavenumbers is typical for hydrogen bonding of the SiOHAl groups[50–52]. To exclude the possibility of chemically anchoring this group at the oxygen of the BAS, that is, that the $Si(OH)_x$ replaces the proton of the bridging hydroxyl group linking an Al–O tetrahedron, we use the adsorption of pyridine, which is known to form pyridinium ions with BAS[53–55].

Figure 2 shows the infrared spectra of H-MFI and EFSi-MFI samples with varying adsorbed concentrations of pyridine. As H-MFI was exposed to aliquots of pyridine, the characteristic band of the SiOHAl groups (3,610 cm^{-1}) decreased with the concomitant appearance of the pyridinium band (1,545 cm^{-1}), which increased in intensity (Fig. 2a). The decrease in the SiOHAl band (that is, the concentration of BAS that are interacting with pyridine) and the intensity of the pyridinium ion band (that is, [HPy^+], the pyridinium ion concentration) for H-MFI were directly proportional (Fig. 2e). This suggests that pyridine adsorbs on all BAS, forming a 1:1 ratio of pyridinium ions and BAS[44].

By contrast, the adsorption of pyridine on the EFSi-MFI samples exhibited two different regimes. Taking EFSi-MF-61% as an example (Fig. 2d,h), after the first aliquots of pyridine were adsorbed, the band

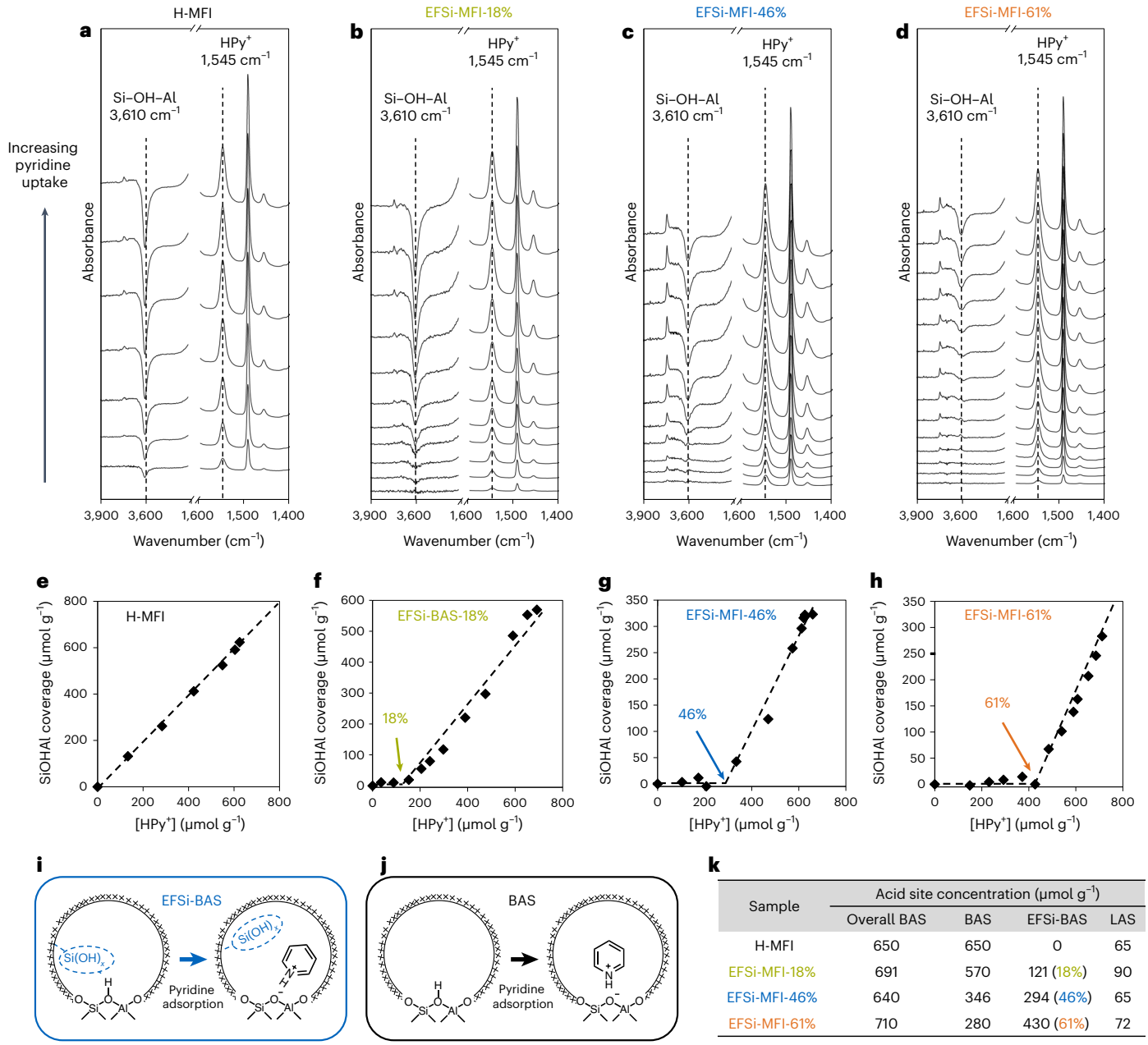

k

Sample	Acid site concentration (μmol g^{-1})			
	Overall BAS	BAS	EFSi-BAS	LAS
H-MFI	650	650	0	65
EFSi-MFI-18%	691	570	121 (18%)	90
EFSi-MFI-46%	640	346	294 (46%)	65
EFSi-MFI-61%	710	280	430 (61%)	72

Fig. 2 | The titration of BAS and EFSi-BAS with pyridine adsorption. a–d, Difference infrared spectra for the OH stretching and NH bending vibration regions of H-MFI (**a**) and EFSi-MFI-18% (**b**), -46% (**c**) and -61% (**d**) with increasing pyridine uptake at 423 K. HPy^+, pyridinium ion. **e–h**, SiOHAl (3,610 cm^{-1}) coverage under different pyridinium ion concentrations on H-MFI (**e**) and EFSi-MFI-18% (**f**), -46% (**g**) and -61% (**h**). The pyridinium ion concentration was determined from the peak area of the 1,545 cm^{-1} band; SiOHAl coverage was determined from the peak area of the 3,610 cm^{-1} band. **i**,**j**, Schematic illustration of pyridine adsorption on EFSi-BAS (**i**) and BAS (**j**). **k**, Concentration of acid sites on H-MFI and the EFSi-MFI samples determined via pyridine titration. LAS, Lewis acid sites.

of the SiOHAl groups (3,610 cm^{-1}) remained unchanged up to the formation of [HPy^+] = 430 μmol g^{-1}. Only subsequently did the SiOHAl band begin to decrease in intensity. The coverage of SiOHAl (that is, the decrease in intensity) increased linearly with the pyridinium ion concentration, following a 1:1 ratio. The EFSi-MFI-18% (Fig. 2b,f) and EFSi-MFI-46% (Fig. 2c,g) samples followed the same trend, with the turning thresholds at 121 and 294 μmol per g pyridinium ions. These concentrations are equal to the concentrations of the EFSi loading (130 μmol Si per g H-MFI on EFSi-MFI-18%; 300 μmol Si per g H-MFI on EFSi-MFI-46%; 430 μmol Si per g H-MFI on EFSi-MFI-61%).

These two adsorption regimes suggest two different types of acid site on EFSi-MFI. Pyridine was first adsorbed on the BAS having an adjacent EFSi (Fig. 2i); this type of acid site was named EFSi-BAS (the SiOHAl band at 3,610 cm^{-1} being hydrogen bonded, shifting to a lower wavenumber). The second regime was identical to the parent BAS, which has the SiOHAl band at 3,610 cm^{-1} (Fig. 2j). Thus, each adsorbed pyridine formed a pyridinium ion, reducing proportionately the intensity of the SiOHAl band at 3,610 cm^{-1}. The concentrations of EFSi-BAS and BAS were quantified via the corresponding pyridine uptake in the two regimes (Fig. 2e–h,k), that is, for the EFSi-MFI-61% sample, the first 430 μmol per g pyridinium ions were formed on EFSi-BAS and the latter 280 μmol per g pyridinium ions were formed on BAS. This suggests that the EFSi species are not chemically bound to BAS, but rather break up a Si–O–Si bridge forming a silanol nest with the $Si(OH)_x$ group attached.

The preferential adsorption of pyridine on EFSi-BAS may be attributed either to the higher acid strength of EFSi-BAS compared with BAS

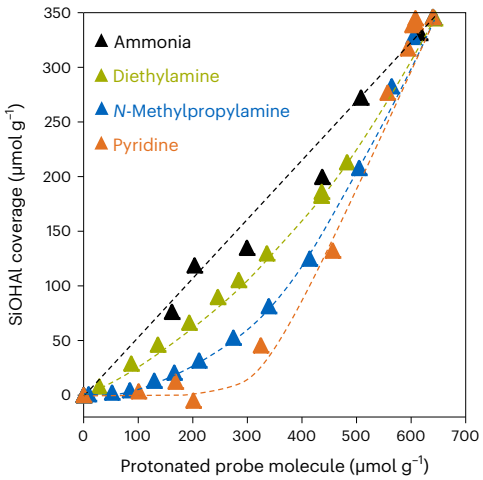

Fig. 3 | Adsorption of different probe base molecules on EFSi-MFI-46% at 423 K. SiOHAl coverage (determined from the areal decrease of the 3,610 cm^{-1} band of the infrared spectra) under different concentrations of protonated probe molecules, that is, ammonium ions, diethylaminium ions, *N*-methylpropylaminium ions and pyridinium ions.

or to an additional interaction between EFSi and the aryl ring on the pyridine molecule stabilizing the adsorbed state. To test these two possibilities, ammonia, diethylamine and *N*-methylpropylamine were used as probe molecules to titrate the acid sites on EFSi-MFI-46%. For ammonia adsorption (Fig. 3) the SiOHAl coverage increased linearly with the concentration of formed ammonium ion. Because the total concentration of ammonium ion was identical to the total concentration of pyridinium ions, the result demonstrates the stochastic adsorption of ammonia on both BAS and EFSi-BAS, indicating also the similar acid strength of BAS and EFSi-BAS. This is further supported by the results of ammonia temperature-programmed desorption (TPD), which show the overlapping desorption curves of H-MFI and all EFSi-MFI samples (Supplementary Fig. 5). However, for base molecules with increasingly bulky alkyl or aryl parts, the SiOHAl coverage differs from the concentration of sorbed protonated molecules (Fig. 3). Stronger preferential adsorption on EFSi-BAS correlates with the bulkiness of the adsorbed base molecules, that is, pyridine > *N*-methylpropylamine > diethylamine. Combining these results leads to the conclusion that the presence of EFSi influences the environment of the BAS in its proximity without changing the acid strength. We hypothesize the stronger interaction to be the result of additional van der Waals interactions with the organic alkyl/aryl part.

To further investigate if such an additional van der Waals interaction is also pronounced with a weakly basic guest molecule, *n*-pentane was adsorbed on H-MFI and the EFSi-MFI samples and characterized using infrared spectroscopy. On H-MFI (Fig. 4a and Supplementary Fig. 6a), the intensity of SiOHAl vibration at 3,610 cm^{-1} decreased with increasing pentane pressure, while a new band at 3,484 cm^{-1} increased in intensity. This band is attributed to the perturbed band of SiOHAl interacting with *n*-pentane via hydrogen bonding. With increasing pressure this band gradually shifted to 3,474 cm^{-1}, indicating a stronger polarization of the bridging OH group through the interaction with an additional pentane molecule[56].

The decrease in the SiOHAl band was also observed with the EFSi-MFI samples; however, the band at 3,484 cm^{-1} was much broader compared with that on H-MFI (Fig. 4b and Supplementary Fig. 6b–d). This implies that an alternative and stronger hydrogen bonding of SiOHAl groups is induced by the presence of EFSi.

To differentiate between the hydrogen-bonded SiOHAl groups, pyridine was selectively adsorbed on EFSi-BAS, while leaving the unmodified BAS in EFSi-MFI accessible. Pentane adsorbed on this sample led to the band at 3,484 cm^{-1} being nearly identical to that of pentane adsorbed on the parent H-MFI (Fig. 4c). Thus, we conclude that unmodified BAS are unaffected by the generation of the new site. The difference in the spectra with and without pyridine blocking the EFSi-BAS enables the infrared spectrum for the hydrogen bonding of *n*-pentane on EFSi-BAS to be accessed (Fig. 4d). This difference spectrum shows that the adsorption of *n*-pentane on EFSi-BAS does not lead a decrease in the band at 3,610 cm^{-1}, causing a pair of bands of hydrogen-bonded OH groups at 3,408 cm^{-1} and 3,538 cm^{-1}, which are attributed to hydrogen-bonded EFSi–SiOHAl and EFSi–OH, respectively. It also shows a marked increase in the intensity of the Si–OH band at 3,735 cm^{-1} and the band at 3,710 cm^{-1} that is typical for SiOH groups interacting with an alkane.

Thus, we conclude that EFSi-BAS consist of a bridging EFSi–SiOHAl group interacting with EFSi–OH via hydrogen bonding (Fig. 4e). Before *n*-pentane adsorption, EFSi–OH and EFSi–SiOHAl interact via hydrogen bonding, which redshifts and broadens both bands, making them hardly observable. The sorbed *n*-pentane perturbs the hydrogen-bonded bridging EFSi–SiOHAl group and EFSi–OH and leads to the bands at 3,408 and 3,538 cm^{-1}, respectively. The lower wavenumber of the perturbed EFSi–SiOHAl group (3,408 cm^{-1}), with respect to perturbed SiOHAl (3,474 cm^{-1}), points to a stronger polarization of the EFSi–SiOHAl group by the adjacent EFSi.

Density functional theory (DFT) calculations help to further interrogate the two adsorption sites (see Supplementary Note 1). The simulated results indicate that the O–H bond length of the BAS increased upon interaction with the EFSi–OH and leads to the experimentally observed decrease in the intensity of the band 3,610 cm^{-1}. The simulated adsorption results of *n*-pentane, ammonia, diethylamine, *N*-methylpropylamine and pyridine also indicated that the preferential adsorption is only favoured if the proton is transferred to the sorbate. Bulkier molecules are stabilized to a greater extent on EFSi-BAS via additional interactions between the alkyl/aryl groups in line with the experimental findings.

Thus we conclude that the grafted EFSi is located selectively in the vicinity of BAS and interact via hydrogen bonding. The adsorption strength is promoted by the proximate EFSi for strong base molecules with alkyl chains or aryl rings such as alkylamines and pyridine. The stronger sorption is caused by van der Waals interactions between the EFSi species and the alkyl/aryl groups of the protonated adsorbed molecules on the BAS.

Catalytic activity of EFSi-BAS in *n*-pentane cracking

After demonstrating the stabilization of alkylaminium cations through the confinement of proximate EFSi to the BAS, we hypothesize that such an effect is transferable to the stability of the alkyl carbocations and should, hence, be reflected in the rates of BAS-catalysed reactions such as cracking[57], dehydrogenation[58] and alkylation[59]. Here, the protolytic cracking and dehydrogenation of *n*-pentane was chosen as a model reaction to test this hypothesis. The mechanism for this reaction has been well established and serves as a benchmark[7,29,30]. In our previous work, *n*-pentane showed similar adsorption enthalpy (ΔH°_{ads}) and entropy (ΔS°_{ads}) values on H-ZSM-5 zeolites with or without EFAl species[30]; in addition, identical values for the adsorption enthalpy of *n*-pentane were found (approximately −65 kJ mol^{-1}; Supplementary Fig. 15 and Supplementary Table 6) on all the samples with EFSi in the present work. The identical adsorption properties of *n*-pentane suggest a similar adsorption state for *n*-pentane on normal BAS, EFSi-BAS and EFAl-BAS (BAS having an adjacent EFAl), indicating the sole importance of the transition states for the specific reaction rates.

The BAS-catalysed protolytic *n*-pentane conversion proceeds via three different cracking pathways, that is, forming methane plus butene (P1, $C_1 + C_4^=$), ethane plus propene (P2, $C_2 + C_3^=$) and propane plus ethene (P3, $C_3 + C_2^=$), as well as one pathway for dehydrogenation (Fig. 5a), through different transition states. As shown in Fig. 5a, both P1 and P3 pathways go through a C2 carbonium-ion-like transition

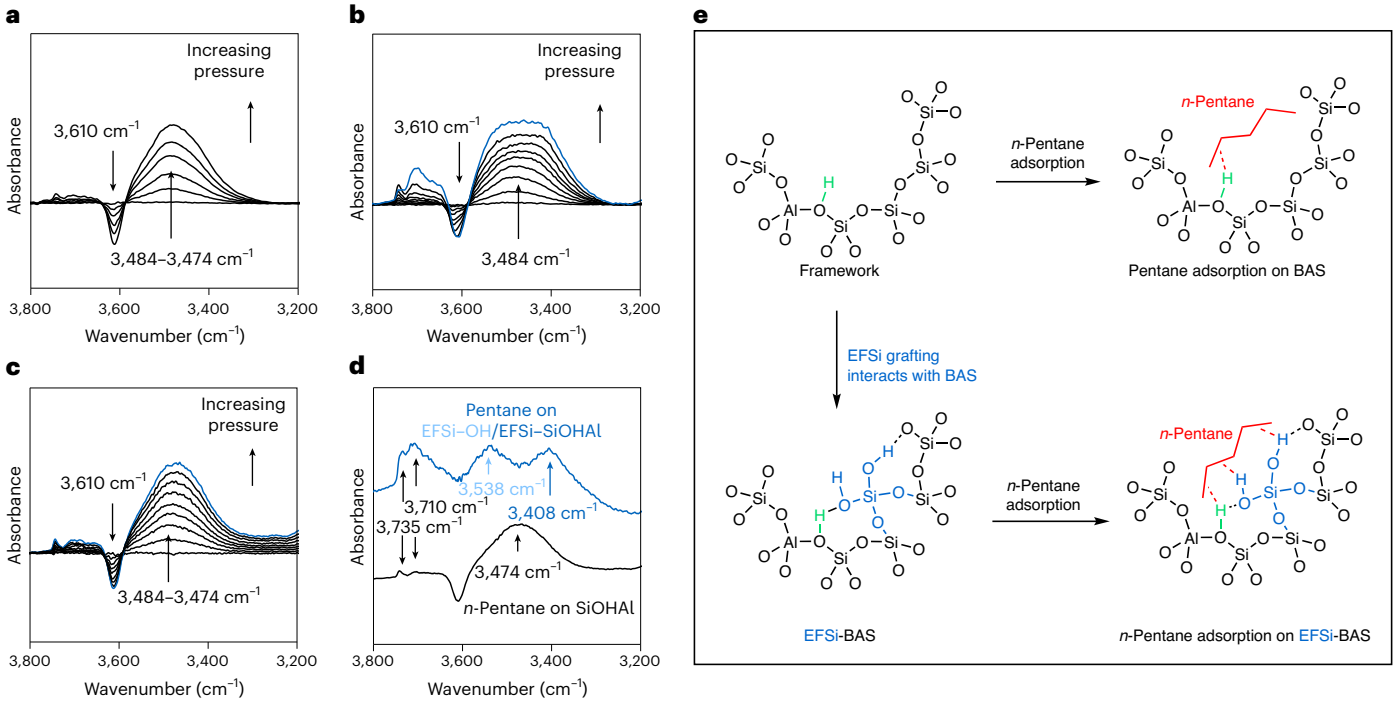

Fig. 4 | *n*-Pentane adsorption on H-MFI and EFSi-MFI-46%. a–**c**, Difference spectra in the OH stretching vibration region for H-MFI (**a**), EFSi-MFI-46% (**b**) and pre-pyridine-titrated EFSi-MFI-46% (**c**) with sorbed *n*-pentane at 333 K under increasing *n*-pentane pressures up to a coverage of approximately 346 µmol SiOHAl per g catalyst, where the SiOHAl coverage was determined from the peak area of the 3,610 cm^{-1} band. **d**, Difference spectra between **b** and **c** showing the spectra of *n*-pentane on EFSi–SiOHAl (blue), with the difference spectra of *n*-pentane on SiOHAl (black) as reference. **e**, Proposed structures of grafted EFSi, EFSi-BAS and *n*-pentane adsorption on BAS and EFSi-BAS.

Table 1 | Adsorption enthalpy values for *N*-methylpropylamine (CNCCC) and diethylamine (CCNCC) on normal BAS and EFSi-BAS at 423 K

Entry	Active site	ΔH°_{ads} (kJ mol^{-1})	
		CNCCC	CCNCC
1	BAS	−226	−217
2	EFSi-BAS	−257	−237
3	Difference (entry 2 − entry 1)	−31	−20

state (respectively, C···C^{+}–C–C–C and C–C^{+}···C–C–C, or CC^{+}CC for short), while the P2 pathway passes through a C3 carbonium-ion-like transition state (C–C···C^{+}–C–C, or CCC^{+}CC for short). These transition states are now analogized by *N*-methylpropylamine and diethylamine binding with the acid site. The adsorption of *N*-methylpropylamine (CNCCC) and diethylamine (CCNCC) on the acid site forms the *N*-methylpropylaminium ion (CN^{+}CCC) and diethylaminium ion (CCN^{+}CC), respectively, which imitate the C2 carbonium-ion-like transition state (CC^{+}CCC) for P1/P3 and the C3 carbonium-ion-like transition state (CCC^{+}CC) for P2 (Supplementary Fig. 16) having similar structures and an identical position of the positive charges.

As discussed, CNCCC and CCNCC showed preferential adsorption on EFSi-BAS compared with BAS (Fig. 3), indicating the formation of more stabilized protonated species of CN^{+}CCC and CCN^{+}CC, respectively, on EFSi-BAS compared with normal BAS. The adsorption enthalpy values of CNCCC and CCNCC were, respectively, −226 and −217 kJ mol^{-1} on normal BAS and −257 and −237 kJ mol^{-1}, respectively, on EFSi-BAS (Table 1; see also Supplementary Note 3). The enthalpic stabilization of CN^{+}CCC and CCN^{+}CC by the presence of EFSi led us to hypothesize a similar impact on the CC^{+}CCC and CCC^{+}CC transition states, leading to a lower enthalpic barrier of *n*-pentane cracking and dehydrogenation and higher turnover frequency (TOF) values on EFSi-BAS compared with normal BAS.

The reaction of *n*-pentane showed first-order kinetics in all pathways on H-MFI and the EFSi-MFI samples and was stable during the time studied (Supplementary Figs. 10–12). The TOF values of *n*-pentane on the BAS of H-MFI (Supplementary Table 3) for overall cracking and dehydrogenation at 753 K and 20 mbar of *n*-pentane were, respectively, 0.47×10^{-3} s^{-1} and 0.32×10^{-3} s^{-1}, that is, similar to those reported in our previous study[30]. The EFSi-MFI samples showed higher TOF values in overall cracking as well as in all individual cracking pathways, increasing linearly with the concentration of EFSi-BAS, whereas the dehydrogenation rates were identical for all samples studied (Fig. 5b, Supplementary Fig. 13 and Supplementary Tables 3 and 4). The observed reaction rate on EFSi-MFI involves the contribution from both BAS and EFSi-BAS; the specific contributions were evaluated via extrapolation (Fig. 5b). Compared with BAS, the EFSi-BAS had a higher TOF (0.47×10^{-3} s^{-1} versus 1.1×10^{-3} s^{-1} at 753 K, respectively), whereas for dehydrogenation it was barely affected by EFSi at 753 K and decreased slightly when above 773 K (Supplementary Fig. 13 and Supplementary Tables 3 and 4).

The TOF values at different temperatures for both BAS and EFSi-BAS (Supplementary Tables 3 and 4) together with the identical adsorption enthalpy and entropy of *n*-pentane (Supplementary Table 6) were used to determine the intrinsic activation enthalpy ($\Delta H^{\ddagger\circ}_{int}$) and entropy ($\Delta S^{\ddagger\circ}_{int}$) values (Table 2; see more calculation details in Supplementary Note 2). Compared with the BAS, the $\Delta H^{\ddagger\circ}_{int}$ for the overall cracking was 36 kJ mol^{-1} lower on EFSi-BAS, and for the dehydrogenation pathway it was 50 kJ mol^{-1} lower. The lower $\Delta H^{\ddagger\circ}_{int}$ with EFSi-BAS is concluded to represent an enthalpic stabilization of the transition state by the presence of EFSi. The lower $\Delta S^{\ddagger\circ}_{int}$ with EFSi-BAS suggests that the formed carbonium ion in the transition state is bound tighter to the zeolite than for the parent H-MFI.

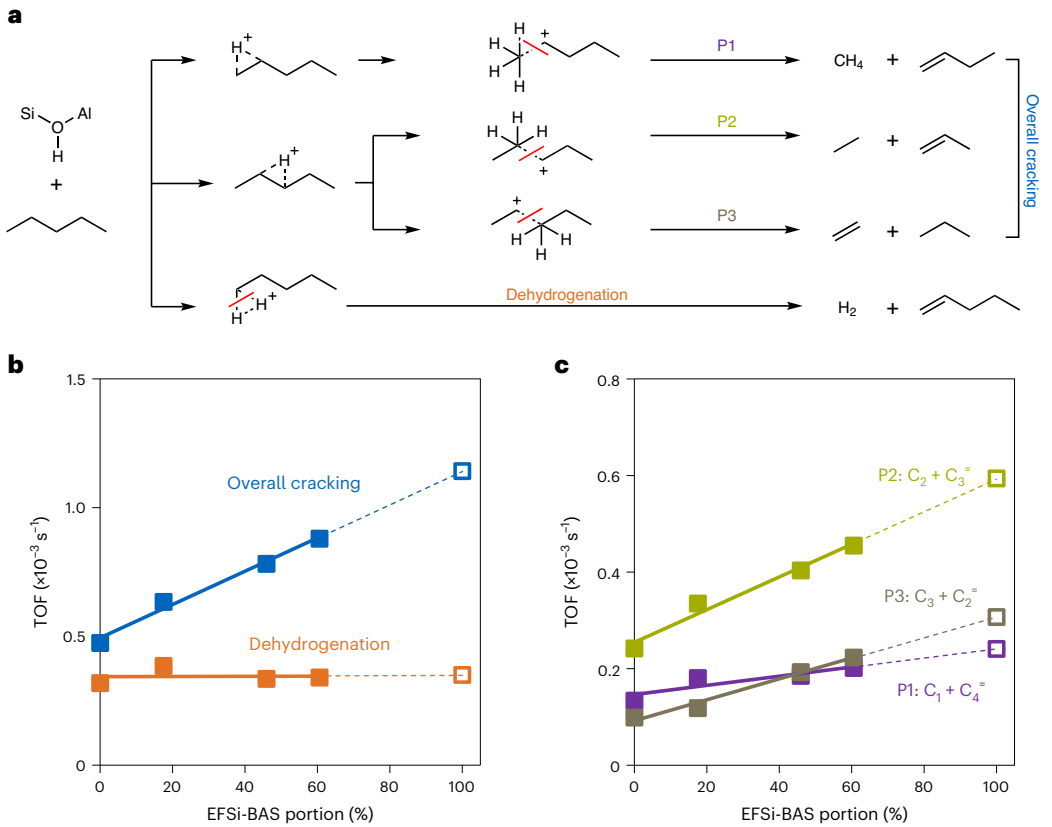

Fig. 5 | BAS-catalysed protolytic *n*-pentane cracking and dehydrogenation on zeolites. a, Reaction pathways for BAS-catalysed protolytic *n*-pentane cracking and dehydrogenation on zeolites. The red line indicates the location of the bond scission. The P1, P2 and P3 cracking pathways of *n*-pentane are illustrated as going through the C2 or C3 carbonium ion. For dehydrogenation, the position is chosen only for illustrative reasons. **b**,**c**, TOF of overall cracking and dehydrogenation (**b**) and different cracking pathways (**c**) as a function of the EFSi-BAS portion of the total BAS on the samples. Reaction temperature, 753 K; *n*-pentane pressure, 20 mbar. Solid symbols denote the experimentally measured TOF; hollow symbols denote the TOF extrapolated to an EFSi-BAS portion of 100%.

Table 2 | Intrinsic activation enthalpy and entropy of *n*-pentane cracking and dehydrogenation on BAS and EFSi-BAS

Entry	Active site	$\Delta H_{int}^{\ddagger o}$ (kJ mol^{-1})				
		P1	P2	P3	OC[a]	D[b]
1	BAS	210±5	171±2	209±5	191±2	209±5
2	EFSi-BAS	159±3	147±2	167±12	155±4	159±10
3	Difference[c]	−51±6	−24±3	−42±13	−36±4	−50±11
		$\Delta S_{int}^{\ddagger o}$ (J mol^{-1} K^{-1})				
4	BAS	19±9	−28±7	15±9	5±7	26±8
5	EFSi-BAS	−43±5	−51±3	−31±11	−35±5	−37±8
6	Difference[c]	−62±10	−23±7	−46±14	−40±9	−63±11

[a]Overall cracking. [b]Dehydrogenation. [c]Difference value between EFSi-BAS and BAS.

Interestingly, the presence of EFSi in proximity to the BAS leads to a substantially larger decrease in $\Delta H_{int}^{\ddagger o}$ for the P1 and P3 pathways (51 kJ mol^{-1} and 42 kJ mol^{-1}, respectively; Table 2, entry 3), whereas the decrease in the P2 pathway is smaller (24 kJ mol^{-1}). This is in line with the observed larger decrease in the adsorption enthalpy of CN^{+}CCC on EFSi-BAS (−31 kJ mol^{-1}; Table 1, entry 3) than that of CCN^{+}CC (−20 kJ mol^{-1}; Table 1, entry 3), suggesting the larger enthalpic stabilization of the C2 carbonium-ion-like transition state (CC^{+}CCC) in the P1 and P3 cracking pathways than that of the C3 carbonium-ion-like transition state (CCC^{+}CC) in the P2 cracking pathway.

These results are consistent with the hypothesis that the proximate EFSi enthalpically stabilizes a positively charged species, for example, a protonated alkylamine, protonated pyridine or protolytic cracking transition state, on the BAS via a more confined environment. The varying enthalpic stabilization of the specific transition states leads to different promotion of the TOF values along the correlated reaction pathways of *n*-pentane cracking. However, the opposite energetic change of the *n*-pentane cracking and dehydrogenation reaction on EFSi-BAS compared with EFAl-BAS in our previous work suggests a very different influence of these two extra-lattice species on the reaction path and will require further studies.

Comparison between EFAl-BAS and EFSi-BAS

While EFAl in proximity to BAS increases the reaction rate for *n*-pentane cracking approximately 50-fold (Fig. 6a), the impact by EFSi is lower[29,30]. The reason behind the specific promotion effect needs to be discussed to understand how different extra-framework species influence the catalytic activity of the proximate acid site. Both extra-lattice species impact the activation enthalpy and entropy differently (the identical state of sorbed reactants on all sites shows that only the transition states change; Supplementary Table 6). Figure 6b,c compares the activation enthalpy and entropy values on BAS, EFAl-BAS and EFSi-BAS, which represent the enthalpies and entropies of the corresponding transition states. Compared with BAS, EFAl-BAS shows an increase in both the activation enthalpy and entropy, whereas both are lower on EFSi-BAS. As we conclude that the strongly entropy-driven lowering of the standard

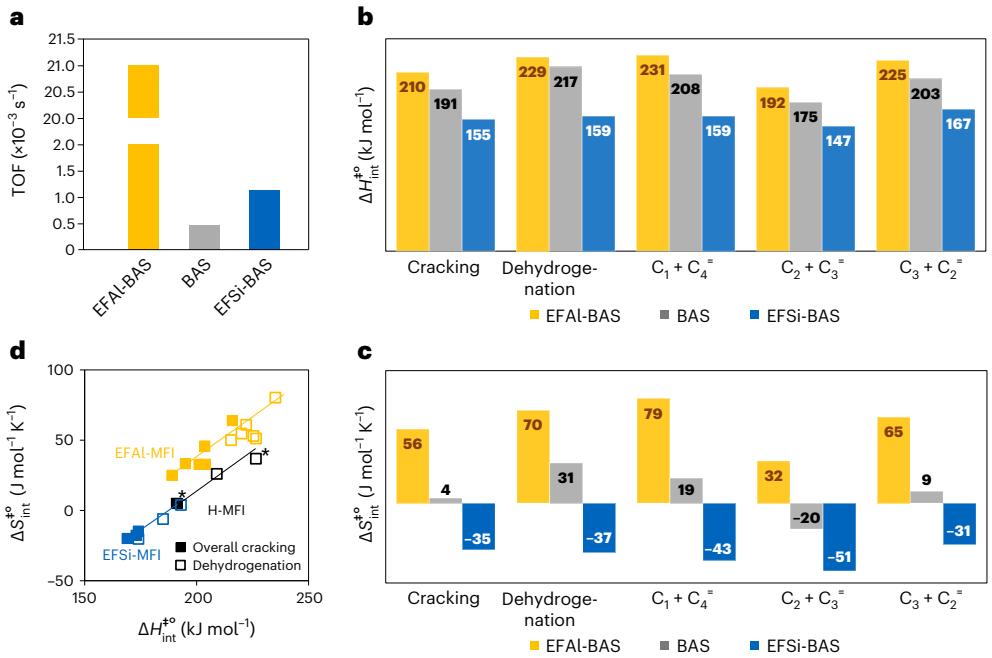

Fig. 6 | Comparison between BAS, EFAl-BAS and EFSi-BAS. a, TOF values for overall cracking on BAS, EFAl-BAS and EFSi-BAS at 753 K. **b**,**c**, Intrinsic activation enthalpy (**b**) and entropy (**c**) data for *n*-pentane cracking and dehydrogenation on BAS, EFAl-BAS and EFSi-BAS. Data for BAS are the average value of the measured data in this work and the reported data from ref. [30]. **d**, Correlation of intrinsic activation entropy and enthalpy for *n*-pentane cracking and dehydrogenation on H-MFI, EFAl-MFI and EFSi-MFI. Data points for H-MFI marked with an asterisk and data for EFAl-BAS/EFAl-MFI are from ref. [30]; other points show the data measured in this work.

transition free energy by EFAl indicates a later transition state, the decrease of the transition enthalpy (and entropy) for the EFSi-catalysed path suggests an earlier, but tighter, bound transition state.

The different influences of EFAl and EFSi are manifested clearly in Fig. 6d by the two compensation lines for the EFSi-MFI and EFAl-MFI samples. The EFSi-MFI samples remain aligned with the correlation of unmodified H-MFI. The compensation line for the EFAl-MFI samples, however, is shifted upwards with respect to the transition entropy, suggesting a change in the reaction pathway via the stabilization of a very late transition state. We hypothesize that this late transition state with the EFAl-MFI samples is caused by better stabilization of the leaving alkane and the formed primary carbenium ion, or a weaker interaction of the transition state with the bridging oxygen atoms of the BAS[60]. Further studies to analyse these differences are in progress.

Conclusions

A neighbouring pair of a bridging OH group (SiOHAl) and an Si(OH)$_x$ group or silanol nest have been synthesized using a stepwise anchoring approach. Experiments and DFT simulations show that the binding of pyridine and alkylamines is stronger on these EFSi-BAS sites than on the parent BAS, whereas that of ammonia is identical. The stronger binding of pyridine and alkylamines is attributed to a more constrained environment that is created by the grafted EFSi groups, introducing additional van der Waals interactions with the alkyl or aryl chain of the probe molecule. The combined dispersion and local polarization induced by hydrogen bonding lead, by contrast, to equal strength for *n*-pentane adsorption on the parent and the modified site.

The EFSi-BAS show a higher rate of cracking of *n*-pentane by enthalpically stabilizing the transition state. The enthalpy of the carbonium-ion-like transition state (CC$^+$CCC) associated with the cracking pathways that produce methane and propane as the alkane reaction products, that is, the P1 and P3 cracking pathways, decreased by 42–51 kJ mol^{-1}; by contrast, the transition state (CCC$^+$CC) associated with the pathway that leads to ethane, that is, the P2 cracking pathway, decreased by only 24 kJ mol^{-1}. The dehydrogenation transition enthalpy also decreased by 50 kJ mol^{-1}, but the rate was identical since the enthalpy decrease was compensated by a transition entropy decrease. Using the analogy of the stabilization of alkylaminium ions, we hypothesize that the differences in the cracking rates of the different pathways are caused by steric constraints for the more asymmetric carbonium ions.

The modification of the environment by Si(OH)$_x$ groups leads to sites in which the EFSi enhances the cracking and dehydrogenation of *n*-pentane via the stabilization of an earlier transition state compared with EFAl and is manifested in a lower transition enthalpy and entropy. The identical compensation correlation between entropy and enthalpy for unmodified H-MFI and EFSi-MFI suggests a similar transition state, but a better stabilization is induced for EFSi-BAS. By contrast, for EFAl-BAS, the higher base strength of the oxygen in EFAl induces a later transition state with a substantially higher transition entropy.

This differentiation shows that the activity for the cracking depends strongly on the nature of the stabilization for the carbocation in the transition state, which appears to be far more controlled by the chemical nature of the extra-lattice oxide species than what has so far been discussed. We are currently evaluating synthesis strategies for defined extra-lattice oxide species that can further enhance the cracking rates, beyond those that have been found for alumina and silica species.

Methods

Sample preparation

The parent H-MFI, used as the starting material for EFSi modification, was prepared via the cleaning of a commercial ZSM-5 zeolite (that is, MFI) in its ammonium form (CBV 2314, named NH$_4$-MFI; Zeolyst International) with SiO_2/Al_2O_3 = 23 using ammonium hexafluorosilicate (AHFS) to remove EFAl, following the previously reported procedure[29]. NH$_4$-MFI was added to a solution of AHFS at 353 K (approximately 1 g catalyst per 40 ml solution) and then stirred for 5 h. The solution contained a 3.2-fold excess of AHFS with respect to the Al content of the

zeolite, which was 2.84 g (16 mmol) AHFS for 3.84 g NH_4-MFI (3.8 wt% Al, corresponding to 5 mmol). Afterwards, the sample was separated and washed with hot deionized water (over 353 K) six times and calcined in a stream of synthetic air (100 ml min^{-1}, heating rate 10 K min^{-1}, 823 K) for 5 h. The obtained sample was in its hydrogen form and was designated as H-MFI.

EFSi was introduced into H-MFI by adsorbing $(CH_3)_3SiN(CH_3)_2$ followed by calcination. The H-MFI (approx. 1 g sample per 5 ml solution) was added to a hexane solution of $(CH_3)_3SiN(CH_3)_2$ at room temperature and stirred overnight. The corresponding amount of $(CH_3)_3SiN(CH_3)_2$ in the solution was either 130, 300 or 430 μmol Si per g H-MFI, which was 0.080 g (0.65 mmol), 0.185 g (1.5 mmol) and 0.265 g (2.15 mmol) $(CH_3)_3SiN(CH_3)_2$ for 5 g H-MFI, respectively. Afterwards, the solid sample was washed three times with hexane and calcined in air (100 ml min^{-1}) for 10 h at 823 K with a heating rate of 1 K min^{-1}. The obtained material was designated as EFSi-MFI-*X*% (with *X*% corresponding to the portion of EFSi-BAS on the samples).

Powder X-ray diffraction

The crystalline structure of the catalyst was determined using powder X-ray diffraction. The X-ray diffraction patterns were collected using a PANalytical Empyrean System diffractometer with Cu Kα radiation (λ = 0.1542 nm), operating at 45 kV/40 mA, using a nickel Kβ filter and a solid-state detector (X'Celerator).

Nitrogen physisorption

Specific surface area and micropore volume values were determined from N_2 adsorption–desorption isotherms measured at liquid N_2 temperature (77 K) using a Thermo Scientific Surfer gas adsorption porosimeter. The samples were outgassed under vacuum at 623 K overnight before the adsorption. The micropore volume was calculated using the *t*-plot method. The BET surface area was calculated using data in the relative pressure range of $0.05 < p/p^0 < 0.12$ with a *C* constant of around 360 for all the samples.

Elemental analysis

The elemental composition of the samples was determined via atomic absorption spectroscopy using a Unicam M Series Flame-AAS instrument equipped with an FS 95 auto-sampler and a GF 95 graphite furnace. Samples were dissolved in a mixture of hydrofluoric acid (48%) and nitrohydrochloric acid at its boiling point before the measurements.

^{27}Al magic-angle spinning NMR spectroscopy

All ^{27}Al magic-angle spinning NMR spectra were recorded using a Bruker Avance 500 Ultrashield NMR spectrometer with a magnetic field of 11.75 T corresponding to the Larmor frequency of 130.3 MHz, and the rotor was spun at 12 kHz. A total of 2,400 spectra were accumulated in a single pulse sequence with a pulse width of 1.16 μs and the relaxation delay of 2 s. Before the measurements, all the samples were hydrated in H_2O (42 mbar) for at least 48 h and then packed into ZrO_2 rotors.

Titration of acid sites with pyridine

Infrared spectroscopy was used to determine the acid-site concentrations of zeolites using pyridine as the probe molecule. All spectra were collected at 423 K using a Nicolet 5700 Fourier-transform infrared (FT-IR) spectrometer at a resolution of 4 cm^{-1}. Zeolites were pressed into wafers and pre-treated under vacuum (at a partial pressure, *p*, of $<10^{-5}$ mbar) at 723 K for 1 h. Then they were exposed to a pulse of pyridine (~3×10^{-2} mbar) for 10 min. After outgassing for 20 min to remove physisorbed pyridine, the spectrum was collected. A series of spectra under different coverages of BAS were received by repeating this procedure until all the BAS had been titrated by pyridine. The concentration of total BAS was quantified based on the area of the band at 1,545 cm^{-1} normalized to the wafer weight[61]. Using a known integrated molar extinction coefficient of 0.73 cm μmol^{-1} for the band at 1,545 cm^{-1}, the integrated molar extinction coefficient for SiOHAl at 3,610 cm^{-1} can be calculated from the slope of the peak area decrease for 3,610 cm^{-1} as a function of the peak area increase of the 1,545 cm^{-1} band on H-MFI, which was found to be 2.65 cm μmol^{-1}.

Titration of acid sites with ammonia

Infrared spectroscopy was used to determine the acid-site concentrations of zeolites with ammonia as the probe molecule. All spectra were collected at 423 K using the Nicolet 5700 FT-IR spectrometer at a resolution of 4 cm^{-1}. Zeolites were pressed into wafers and pre-treated under vacuum ($p < 10^{-5}$ mbar) at 723 K for 1 h. Then they were exposed to a pulse of ammonia for 10 min. After outgassing for 20 min to remove physisorbed ammonia, the spectrum was collected. A series of spectra under different coverages of BAS were obtained by repeating this procedure until all the BAS had been titrated by ammonia.

The TPD of ammonia was performed using a six-fold parallel reactor system. The solid catalysts were activated under vacuum at 723 K with a heating rate of 10 K min^{-1} for 1 h. Ammonia was adsorbed with a partial pressure of 1 mbar at 353 K. Subsequently, the samples were outgassed under vacuum for 2 h to remove physisorbed molecules. For the TPD measurements, the samples were heated under vacuum from 353 to 1,033 K with a temperature increment of 10 K min^{-1} to desorb ammonia. The desorbed ammonia (channel mass-to-charge ratio, m/z = 17) was monitored via mass spectrometry (Balzers QME 200). For acid-site quantification, a reference (H-ZSM-5 with Si/Al = 45; Clariant) with a known acidity (400 μmol g^{-1}) was used to calibrate the signal.

Adsorption of *N*-methylpropylamine and diethylamine

Infrared spectroscopy of adsorbed *N*-methylpropylamine and diethylamine was used to identify their respective adsorption sites and formed species on H-MFI and the EFSi-MFI samples. All spectra were collected at 423 K using a Vertex 70 spectrometer from Bruker Optics at a resolution of 4 cm^{-1}. Zeolite wafers were loaded into an infrared cell connected to a vacuum system. It was first pre-treated under vacuum ($p < 10^{-5}$ mbar) at 723 K for 1 h and then cooled to 423 K. Then it was exposed to a pulse of N-methylpropylamine or diethylamine (~3×10^{-2} mbar) for 10 min. After outgassing for 20 min to remove any physisorbed amine, the spectrum was collected. A series of spectra under different uptakes were obtained by repeating this procedure until all the BAS had been covered.

The adsorption of *N*-methylpropylamine and diethylamine on H-MFI and EFSi-MFI samples was also measured gravimetrically using a microbalance in a Seteram TG-DSC 111 calorimeter connected to a high-vacuum system. After pre-treatment of the sample (20 mg) at 723 K for 1 h under vacuum ($p < 10^{-4}$ mbar), it was cooled to 423 K. Afterwards, *N*-methylpropylamine or diethylamine was introduced into the system as a pulse. By controlling the dosing pressure and exposure time, approximately 0.08 mmol amine per mmol BAS was adsorbed in each pulse. The amine uptake was determined by the increase in the sample weight, and the released heat was obtained via integration of the heat flux.

Calculation of concentration of protonated probe molecules and coverage of BAS using infrared spectra

The concentrations of protonated probe molecules were determined using the area of the characteristic band on the infrared spectrum (normalized to the band area of full coverage as 100%; that is, the band at 1,605 cm^{-1} for the ammonium ion, the band at 1,602 cm^{-1} for the diethylaminium ion and the band at 1,608 cm^{-1} for the *N*-methylpropylaminium ion; Supplementary Fig. 18). Similarly, the coverage of BAS (θ_{BAS}) is determined from the areal decrease of the band at 3,610 cm^{-1} (normalized to the initial band area at 3,610 cm^{-1} as 100% for each respective sample). Therefore, with the known concentration of overall BAS ([overall BAS]) and unmodified BAS ([BAS]) determined from pyridine titration, the concentration of covered overall BAS and

BAS are calculated. Their difference is the concentration of covered EFSi-BAS (equation (1)):

$$\theta_{\text{EFSi-BAS}} \times [\text{EFSi} - \text{BAS}] = \theta_{\text{overall BAS}} \times [\text{overall BAS}] - \theta_{\text{BAS}} \times [\text{BAS}] \quad (1)$$

where $\theta_{\text{EFSi-BAS}}$ represents the coverage of EFSi-BAS under a certain uptake of probe molecules and [EFSi-BAS] is the concentration of EFSi-BAS.

Adsorption of *n*-pentane

The adsorption isotherms of *n*-pentane on H-MFI and the EFSi-MFI samples were measured using a Seteram TG-DSC 111 calorimeter connected to a high-vacuum system. The corresponding sample (~20 mg) was placed in a quartz sample holder and activated at 723 K for 1 h under vacuum ($p < 10^{-4}$ mbar) with a heating rate of 10 K min^{-1}. After the samples had cooled to 333 K, *n*-pentane was introduced into the system via controlled dosing. The adsorbed *n*-pentane was determined in small pressure steps from 1×10^{-3} mbar to 40 mbar. The *n*-pentane uptake was determined via the increase of sample weight, and the released heat was obtained by integration of the heat flux signal.

The adsorption isotherms were analysed in terms of the Langmuir adsorption model, as in equation (2):

$$n = \frac{n_{\max} \times K^{\circ}_{\text{ads}} \times p}{1 + K^{\circ}_{\text{ads}} \times p} \quad (2)$$

where n is the amount of adsorbate on the sample, $n_{\max}$ is the maximum uptake of the adsorbate, K denotes the equilibrium constant of adsorption and p is the normalized pressure (referenced to $p^{\circ} = 1$ bar). The adsorption entropy ($\Delta S^{\circ}_{\text{ads}}$) was calculated using equation (3):

$$\Delta S^{\circ}_{\text{ads}} = \frac{\Delta H^{\circ}_{\text{ads}}}{T} + R \ln K^{\circ}_{\text{ads}} \quad (3)$$

where $\Delta H^{\circ}_{\text{ads}}$ is the standard adsorption enthalpy, T is the absolute temperature and R is the universal gas constant.

Infrared spectroscopy was conducted using a Bruker Optics Vertex 70 spectrometer at a resolution of 4 cm^{-1}. Samples were prepared as self-supporting wafers and outgassed under vacuum ($p < 10^{-5}$ mbar) at 723 K for 1 h with a heating rate of 10 K min^{-1}. After cooling to 333 K, *n*-pentane was introduced into the system via controlled dosing. The adsorbed *n*-pentane was determined in small pressure steps from 1×10^{-3} mbar to 10 mbar. A series of spectra were collected under different pressures of *n*-pentane until all the BAS had been perturbed.

Reaction of *n*-pentane cracking and dehydrogenation

The protolytic cracking and dehydrogenation of *n*-pentane on H-MFI and the EFSi-MFI samples was conducted at ambient pressure using a tubular flow reactor with a quartz tube with an internal diameter of 7 mm. Catalyst pellets (300–500 µm) were activated in situ at 803 K with a heating ramp of 2 K min^{-1} for 2 h in a flow of synthetic air (30 ml min^{-1}) and then flushed for 30 min with N_2 (100 ml min^{-1}). The reactant stream was introduced into the reactor via an evaporator and then by N_2 as a carrier gas. The reaction conditions of a low catalyst loading (approximately 400 mg catalyst), a low pentane partial pressure (20 mbar) and a high temperature range (753–793 K) were used to follow the monomolecular cracking and dehydrogenation pathways. Reactant and products were separated and analysed via on-line chromatographic measurements (Supelco Q-Plot, capillary column: 30 m × 0.53 mm × 2.0 µm) using a flame ionization detector. The calculation details are in Supplementary Note 2.

Computational details

The restricted Kohn–Sham DFT cluster calculations were performed using the Orca package version 4.2[62]. We performed calculations using two exchange–correlation functionals with the generalized gradient approximation (GGA), that is, BP86 and PBE, and two hybrid GGA functionals, that is, B3LYP and PBE0[63–66]. All-electron Ahlrichs def2 basis sets with double-zeta polarization functions (def2-SVP) were used for geometry optimization, and all-electron Ahlrichs def2 basis sets with triple-zeta polarization functions (def2-TZVP) with a denser integration grid were used for estimating the electronic charges on the adsorbed species[67,68]. The charges were estimated via Hirshfeld population analysis as implemented in Orca. The GGA functionals were employed with resolution-of-identity (RI) approximations, whereas the hybrid functionals were used with RIJCOSX approximation to speed up the calculations[69,70]. For this purpose, the general Weigend J auxiliary basis set def2/J was used[71]. The RIJCOSX approximation incorporates the RI approximation for evaluation of the Coulomb matrices and the chain-of-spheres algorithm for the formation of the exchange-type matrices[72]. All core electrons ($1s^2 2s^2 2p^6$ for Al and Si, $1s^2$ for C, O and N, and none for H) were frozen during the calculations. The calculation utilized the atom-pairwise dispersion correction with the Becke–Johnson damping scheme D3BJ[72,73]. The net charge on the cluster (with adsorbed species) was set to zero and the spin multiplicity was set to one (singlet; spin neutral) for all calculations. The sample input files for geometry optimization and electronic property calculations are reported in the Supplementary Information.

The calculations were performed on a 22 T-site MFI cluster representing the straight channel of the MFI framework. First, a 104 atom cluster terminating at the T sites was cut along the straight channels of MFI comprising two co-joined ten-membered rings. The initial structural parameters of the MFI unit cell were obtained from the International Zeolite Association database[74]. The terminating T-site atoms were then replaced with H, and the O–H bond distance was set to 0.97 Å. The resulting cluster was comprised of 22 Si, 56 O and 26 terminating H atoms and was charge neutral. This initial cluster was optimized for use in further calculations. For all geometry optimizations, the terminal H atoms were kept frozen while all other atoms were allowed to relax. The Cartesian coordinates of the initial cluster used in the DFT calculations are reported in the Supplementary Information.

The adsorption of ammonia, diethylamine, *N*-methylpropylamine and *n*-pentane were investigated on two different adsorption sites: (1) BAS; and (2) EFSi-BAS. For simulations on BAS, one Si atom in the ten-membered ring of MFI was replaced with an Al, and one H atom was placed next to an adjacent O at a distance of 0.97 Å. The EFSi site was simulated by replacing an Si–O–Si group with an Si–OSi(OH)$_2$O–Si group. The simulations on EFSi-BAS were performed by placing the BAS and EFSi next to each other. For the simulation with adsorbed species, the adsorbates (ammonia, diethylamine, *N*-methylpropylamine and *n*-pentane) were placed near the BAS proton or the hydroxyl group of EFSi, and the geometry was allowed to relax.

Data availability

All data are available from the corresponding authors upon reasonable request.

References

1. Rahimi, N. & Karimzadeh, R. Catalytic cracking of hydrocarbons over modified ZSM-5 zeolites to produce light olefins: a review. *Appl. Catal. A* **398**, 1–17 (2011).
2. Babitz, S. M. M. et al. Monomolecular cracking of *n*-hexane on Y, MOR, and ZSM-5 zeolites. *Appl. Catal. A* **179**, 71–86 (1999).
3. Weitkamp, J., Jacobs, P. A. & Martens, J. A. Isomerization and hydrocracking of C_9 through C_{16} n-alkanes on Pt/HZSM-5 zeolite. *Appl. Catal.* **8**, 123–141 (1983).
4. Young, L. B., Butter, S. A. & Kaeding, W. W. Shape selective reactions with zeolite catalysts: III. Selectivity in xylene isomerization, toluene-methanol alkylation, and toluene disproportionation over ZSM-5 zeolite catalysts. *J. Catal.* **76**, 418–432 (1982).

5. Xu, B., Sievers, C., Hong, S. B., Prins, R. & van Bokhoven, J. A. Catalytic activity of Brønsted acid sites in zeolites: intrinsic activity, rate-limiting step, and influence of the local structure of the acid sites. *J. Catal.* **244**, 163–168 (2006).
6. Ward, J. W. The nature of active sites on zeolites: V. In situ spectroscopic observations of hydrogen Y zeolite during cumene cracking. *J. Catal.* **11**, 259–260 (1968).
7. Kissin, Y. V. Chemical mechanisms of catalytic cracking over solid acidic catalysts: alkanes and alkenes. *Catal. Rev. Sci. Eng.* **43**, 85–146 (2001).
8. Ozaki, A. & Kimura, K. The effective site on acid catalysts revealed in *n*-butene isomerization. *J. Catal.* **3**, 395–405 (1964).
9. Asuquo, R. A., Edermirth, G. & Lercher, J. A. n-Butane isomerization over acidic mordenite. *J. Catal.* **155**, 376–382 (1995).
10. Feller, A., Guzman, A., Zuazo, I. & Lercher, J. A. On the mechanism of catalyzed isobutane/butene alkylation by zeolites. *J. Catal.* **224**, 80–93 (2004).
11. Naccache, C., Ren, C. F. & Coudurier, G. Strength of acid sites in zeolites using UV-visible spectroscopy: effect of Al content. *Stud. Surf. Sci. Catal.* **49**, 661–668 (1989).
12. Masuda, T., Fujikata, Y., Mukai, S. R. & Hashimoto, K. Changes in catalytic activity of MFI-type zeolites caused by dealumination in a steam atmosphere. *Appl. Catal. A* **172**, 73–83 (1998).
13. Li, S. et al. Brønsted/Lewis acid synergy in dealuminated HY zeolite: a combined solid-state NMR and theoretical calculation study. *J. Am. Chem. Soc.* **129**, 11161–11171 (2007).
14. Chu, C. T. W. & Chang, C. D. Isomorphous substitution in zeolite frameworks. 1. Acidity of surface hydroxyls in [B]-, [Fe]-, [Ga]-, and [Al]-ZSM-5. *J. Phys. Chem.* **89**, 1569–1571 (1985).
15. Losch, P. et al. Proton mobility, intrinsic acid strength, and acid site location in zeolites revealed by varying temperature infrared spectroscopy and density functional theory studies. *J. Am. Chem. Soc.* **140**, 17790–17799 (2018).
16. Jones, A. J., Carr, R. T., Zones, S. I. & Iglesia, E. Acid strength and solvation in catalysis by MFI zeolites and effects of the identity, concentration and location of framework heteroatoms. *J. Catal.* **312**, 58–68 (2014).
17. Ward, J. W. The nature of active sites on zeolites. VIII. Rare earth Y zeolite. *J. Catal.* **13**, 321–327 (1969).
18. Xiaoning, W. et al. Effects of light rare earth on acidity and catalytic performance of HZSM-5 zeolite for catalytic cracking of butane to light olefins. *J. Rare Earths* **25**, 321–328 (2007).
19. Martins, A., Silva, J. M. & Ribeiro, M. F. Influence of rare earth elements on the acid and metal sites of Pt/HBEA catalyst for short chain *n*-alkane hydroisomerization. *Appl. Catal. A* **466**, 293–299 (2013).
20. Sastre, G. & Corma, A. The confinement effect in zeolites. *J. Mol. Catal. A* **305**, 3–7 (2009).
21. Gounder, R. & Iglesia, E. The catalytic diversity of zeolites: confinement and solvation effects within voids of molecular dimensions. *Chem. Commun.* **49**, 3491–3509 (2013).
22. Eder, F. & Lercher, J. A. On the role of the pore size and tortuosity for sorption of alkanes in molecular sieves. *J. Phys. Chem. B* **101**, 1273–1278 (1997).
23. De Moor, B. A., Reyniers, M.-F., Gobin, O. C., Lercher, J. A. & Marin, G. B. Adsorption of C2–C8 n-alkanes in zeolites. *J. Phys. Chem. C* **115**, 1204–1219 (2010).
24. Janda, A., Vlaisavljevich, B., Lin, L. C., Smit, B. & Bell, A. T. Effects of zeolite structural confinement on adsorption thermodynamics and reaction kinetics for monomolecular cracking and dehydrogenation of *n*-butane. *J. Am. Chem. Soc.* **138**, 4739–4756 (2016).
25. Boronat, M. & Corma, A. What is measured when measuring acidity in zeolites with probe molecules? *ACS Catal.* https://doi.org/10.1021/acscatal.8b04317 (2019).
26. Wang, Q., Cui, Z. M., Cao, C. Y. & Song, W. G. 0.3 Å makes the difference: dramatic changes in methanol-to-olefin activities between H-ZSM-12 and H-ZSM-22 zeolites. *J. Phys. Chem. C* **115**, 24987–24992 (2011).
27. Silaghi, M.-C., Chizallet, C. & Raybaud, P. Challenges on molecular aspects of dealumination and desilication of zeolites. *Microporous Mesoporous Mater.* **191**, 82–96 (2014).
28. Silaghi, M.-C., Chizallet, C., Sauer, J. & Raybaud, P. Dealumination mechanisms of zeolites and extra-framework aluminum confinement. *J. Catal.* **339**, 242–255 (2016).
29. Schallmoser, S. et al. Impact of the local environment of Brønsted acid sites in ZSM-5 on the catalytic activity in n-pentane cracking. *J. Catal.* **316**, 93–102 (2014).
30. Zhang, Y. et al. Promotion of protolytic pentane conversion on H-MFI zeolite by proximity of extra-framework aluminum oxide and Brønsted acid sites. *J. Catal.* **370**, 424–433 (2019).
31. Lago, R. M. et al. The nature of the catalytic sites in HZSM-5-activity enhancement. *Stud. Surf. Sci. Catal.* **28**, 677–684 (1986).
32. van Bokhoven, J. A. et al. An explanation for the enhanced activity for light alkane conversion in mildly steam dealuminated mordenite: the dominant role of adsorption. *J. Catal.* **202**, 129–140 (2001).
33. Van Bokhoven, J. A. et al. Observation of a compensation relation for monomolecular alkane cracking by zeolites: the dominant role of reactant sorption. *J. Catal.* **224**, 50–59 (2004).
34. Yu, Z., Wang, Q., Chen, L. & Deng, F. Brønsted/Lewis acid sites synergy in H-MCM-22 zeolite studied by ^{1}H and ^{27}Al DQ-MAS NMR spectroscopy. *Chin. J. Catal.* **33**, 129–139 (2012).
35. Haag, W. O. Catalysis by zeolites—science and technology. *Stud. Surf. Sci. Catal.* **84**, 1375–1394 (1994).
36. Li, S. et al. Probing the spatial proximities among acid sites in dealuminated H-Y zeolite by solid-state NMR spectroscopy. *J. Phys. Chem. C* **112**, 14486–14494 (2008).
37. Gounder, R., Jones, A. J., Carr, R. T. & Iglesia, E. Solvation and acid strength effects on catalysis by faujasite zeolites. *J. Catal.* **286**, 214–223 (2012).
38. Xue, N. et al. Hydrolysis of zeolite framework aluminum and its impact on acid catalyzed alkane reactions. *J. Catal.* **365**, 359–366 (2018).
39. Zheng, J. et al. A periodic DFT study of the synergistic mechanisms between extraframework aluminum species and Brønsted acid sites in HY zeolites. *Ind. Eng. Chem. Res.* **59**, 2736–2744 (2020).
40. O'Connor, C. T., Möller, K. P. & Manstein, H. The effect of silanisation on the catalytic and sorption properties of zeolites. *KONA Powder Part. J.* **25**, 230–236 (2007).
41. Niwa, M., Kato, M., Hattori, T. & Murakami, Y. Fine control of the pore-opening size of zeolite ZSM-5 by chemical vapor deposition of silicon methoxide. *J. Phys. Chem.* **90**, 6233–6237 (1986).
42. Zheng, S., Heydenrych, H. R., Röger, H. P., Jentys, A. & Lercher, J. A. On the enhanced selectivity of HZSM-5 modified by chemical liquid deposition. *Top. Catal.* **22**, 101–106 (2003).
43. Janda, A. & Bell, A. T. Effects of Si/Al ratio on the distribution of framework Al and on the rates of alkane monomolecular cracking and dehydrogenation in H-MFI. *J. Am. Chem. Soc.* **135**, 19193–19207 (2013).
44. Parrillo, D. J., Adamo, A. T., Kokotailo, G. T. & Gorte, R. J. Amine adsorption in H-ZSM-5. *Appl. Catal.* **67**, 107–118 (1990).
45. Ledoux, R. L. & White, J. L. Infrared studies of hydrogen bonding interaction between kaolinite surfaces and intercalated potassium acetate, hydrazine, formamide, and urea. *J. Colloid Interface Sci.* **21**, 127–152 (1966).
46. Vansant, E. F., Van Der Voort, P. & Vrancken, K. C. *Characterization and Chemical Modification of the Silica Surface* Vol. 93, 2960–2970 (Elsevier, 1995).

47. Zecchina, A. et al. Low-temperature Fourier-transform infrared investigation of the interaction of CO with nanosized ZSM5 and silicalite. *J. Chem. Soc. Faraday Trans.* **88**, 2959–2969 (1992).
48. Trombetta, M., Armaroli, T., Gutièrrez Alejandre, A., Ramirez Solis, J. & Busca, G. An FT-IR study of the internal and external surfaces of HZSM5 zeolite. *Appl. Catal. A* **192**, 125–136 (2000).
49. Guisnet, M., Ayrault, P., Coutanceau, C., Alvarez, M. F. & Datka, J. Acid properties of dealuminated beta zeolites studied by IR spectroscopy. *J. Chem. Soc. Faraday Trans.* **93**, 1661–1665 (1997).
50. Zholobenko, V. L., Kustov, L. M., Borovkov, V. Y. & Kazansky, V. B. A new type of acidic hydroxyl groups in ZSM-5 zeolite and in mordenite according to diffuse reflectance IR spectroscopy. *Zeolites* **8**, 175–178 (1988).
51. Jentys, A., Warecka, G., Derewinski, M. & Lercher, J. A. Adsorption of water on ZSM 5 zeolites. *J. Phys. Chem.* **93**, 4837–4843 (1989).
52. Loeffler, E. et al. Study of different states of nonframework aluminum in hydrothermally dealuminated HZSM-5 zeolites using diffuse reflectance IR spectroscopy. *Zeolites* **10**, 266–271 (1990).
53. Kung, M. C. & Kung, H. H. IR studies of NH_3, pyridine, CO, and NO adsorbed on transition metal oxides. *Catal. Rev.* **27**, 425–460 (1985).
54. Chakraborty, B. & Viswanathan, B. Surface acidity of MCM-41 by in situ IR studies of pyridine adsorption. *Catal. Today* **49**, 253–260 (1999).
55. Emeis, C. A. Determination of integrated molar extinction coefficients for infrared absorption bands of pyridine adsorbed on solid acid catalysts. *J. Catal.* **141**, 347–354 (1993).
56. Eder, F., Stockenhuber, M. & Lercher, J. A. Brønsted acid site and pore controlled siting of alkane sorption in acidic molecular sieves. *J. Phys. Chem. B* **101**, 5414–5419 (1997).
57. Kotrel, S., Knözinger, H. & Gates, B. C. The Haag–Dessau mechanism of protolytic cracking of alkanes. *Microporous Mesoporous Mater.* **35**, 11–20 (2000).
58. Al-majnouni, K. A., Yun, J. H. & Lobo, R. F. High-temperature produced catalytic sites selective for *n*-alkane dehydrogenation in acid zeolites: the case of HZSM-5. *ChemCatChem* **3**, 1333–1341 (2011).
59. Liu, Y. et al. Solvent-determined mechanistic pathways in zeolite-H-BEA-catalysed phenol alkylation. *Nat. Catal.* **1**, 141–147 (2018).
60. Janda, A., Vlaisavljevich, B., Lin, L.-C., Smit, B. & Bell, A. T. Effects of zeolite structural confinement on adsorption thermodynamics and reaction kinetics for monomolecular cracking and dehydrogenation of *n*-butane. *J. Am. Chem. Soc.* **138**, 4739–4756 (2016).
61. Jentys, A., Kleestorfer, K. & Vinek, H. Concentration of surface hydroxyl groups on MCM-41. *Microporous Mesoporous Mater.* **27**, 321–328 (1999).
62. Neese, F. The ORCA program system. *WIREs Comput. Mol. Sci.* **2**, 73–78 (2012).
63. Russo, T. V., Martin, R. L. & Hay, P. J. Density functional calculations on first-row transition metals. *J. Chem. Phys.* **101**, 7729–7737 (1994).
64. Tao, J., Perdew, J. P., Tang, H. & Shahi, C. Origin of the size-dependence of the equilibrium van der Waals binding between nanostructures. *J. Chem. Phys.* **148**, 074110 (2018).
65. Miehlich, B., Savin, A., Stoll, H. & Preuss, H. Results obtained with the correlation energy density functionals of Becke and Lee, Yang and Parr. *Chem. Phys. Lett.* **157**, 200–206 (1989).
66. Adamo, C. & Barone, V. Toward reliable density functional methods without adjustable parameters: the PBE0 model. *J. Chem. Phys.* **110**, 6158–6170 (1999).
67. Schäfer, A., Horn, H. & Ahlrichs, R. Fully optimized contracted Gaussian basis sets for atoms Li to Kr. *J. Chem. Phys.* **97**, 2571–2577 (1992).
68. Weigend, F. & Ahlrichs, R. Balanced basis sets of split valence, triple zeta valence and quadruple zeta valence quality for H to Rn: design and assessment of accuracy. *Phys. Chem. Chem. Phys.* **7**, 3297–3305 (2005).
69. Neese, F. An improvement of the resolution of the identity approximation for the formation of the Coulomb matrix. *J. Comput. Chem.* **24**, 1740–1747 (2003).
70. Vahtras, O., Almlöf, J. & Feyereisen, M. W. Integral approximations for LCAO-SCF calculations. *Chem. Phys. Lett.* **213**, 514–518 (1993).
71. Weigend, F. Accurate Coulomb-fitting basis sets for H to Rn. *Phys. Chem. Chem. Phys.* **8**, 1057–1065 (2006).
72. Neese, F., Wennmohs, F., Hansen, A. & Becker, U. Efficient, approximate and parallel Hartree–Fock and hybrid DFT calculations. A 'chain-of-spheres' algorithm for the Hartree–Fock exchange. *Chem. Phys.* **356**, 98–109 (2009).
73. Ehrlich, S., Moellmann, J., Reckien, W., Bredow, T. & Grimme, S. System-dependent dispersion coefficients for the DFT-D3 treatment of adsorption processes on ionic surfaces. *ChemPhysChem* **12**, 3414–3420 (2011).
74. Baerlocher, C. & McCusker, L. B. *Database of Zeolite Structures* (International Zeolite Association Structure Commission, accessed on 09 June 2020); http://www.iza-structure.org/databases/

Acknowledgements

Conceptual work was supported by the US Department of Energy (DOE), Office of Science, Office of Basic Energy Sciences (BES), Division of Chemical Sciences, Geosciences and Biosciences (Impact of catalytically active centers and their environment on rates and thermodynamic states along reaction paths, FWP 47319). We gratefully acknowledge the Leibniz Supercomputing Center for funding this project by providing computing time on their Linux-Cluster. R.Z. is grateful to the Chinese Scholarship Council for financial support. We also acknowledge M. Iqbal and M. Neukamm for technical support concerning the nitrogen physisorption and elemental analysis, respectively.

Author contributions

R.Z. carried out experimental preparation of the catalyst samples, their reactions and characterization. R.K. performed the theoretical calculations. Y.Z., M.S.-S. and R.B.-D. cooperated with the discussion and provided valuable suggestions. Y.L. and J.A.L. supervised the work and provided guidance throughout the project. All authors have given their approval to the final version of the manuscript.

Funding

Open Access funding enabled and organized by Projekt DEAL

Competing interests

The authors declare no competing interests.

Additional information

Supplementary information The online version contains supplementary material available at https://doi.org/10.1038/s41929-022-00906-z.

Correspondence and requests for materials should be addressed to Yue Liu or Johannes A. Lercher.

Peer review information *Nature Catalysis* thanks Xiaolei Fan and the other, anonymous, reviewer(s) for their contribution to the peer review of this work.